HHS Public Access

Author manuscript

Neuroimage. Author manuscript; available in PMC 2019 April 01.

Published in final edited form as:

Neuroimage. 2018 April 01; 169: 227–239. doi:10.1016/j.neuroimage.2017.12.042.

A probabilistic atlas of human brainstem pathways based on connectome imaging data

Yuchun Tang^{a,b,*}, **Wei Sun**^{a,*}, **Arthur W. Toga**^a, **John M. Ringman**^c, and **Yonggang Shi**^{a,**}

^aLaboratory of Neuro Imaging (LONI), USC Stevens Neuroimaging and Informatics Institute, Keck School of Medicine, University of Southern California, Los Angeles, CA, USA

^bResearch Center for Sectional and Imaging Anatomy, Shandong University Cheeloo College of Medicine, Jinan, Shandong, China

^cDepartment of Neurology, Keck School of Medicine, University of Southern California, Los Angeles, CA, USA

Abstract

The brainstem is a critical structure that regulates vital autonomic functions, houses the cranial nerves and their nuclei, relays motor and sensory information between the brain and spinal cord, and modulates cognition, mood, and emotions. As a primary relay center, the fiber pathways of the brainstem include efferent and afferent connections among the cerebral cortex, spinal cord, and cerebellum. While diffusion MRI has been successfully applied to map various brain pathways, its application for the *in vivo* imaging of the brainstem pathways has been limited due to inadequate resolution and large susceptibility-induced distortion artifacts. With the release of high-resolution data from the Human Connectome Project (HCP), there is increasing interest in mapping human brainstem pathways. Previous works relying on HCP data to study brainstem pathways, however, did not consider the prevalence (>80%) of large distortions in the brainstem even after the application of correction procedures from the HCP-Pipeline. They were also limited in the lack of adequate consideration of subject variability in either fiber pathways or region of interests (ROIs) used for bundle reconstruction. To overcome these limitations, we develop in this work a probabilistic atlas of 23 major brainstem bundles using high-quality HCP data passing rigorous quality control. For the large-scale data from the 500-Subject release of HCP, we conducted extensive quality controls to exclude subjects with severe distortions in the brainstem area. After that, we developed a systematic protocol to manually delineate 1300 ROIs on 20 HCP subjects (10 males; 10 females) for the reconstruction of fiber bundles using tractography techniques. Finally, we leveraged our novel connectome modeling techniques including high order fiber orientation distribution (FOD) reconstruction from multi-shell diffusion imaging and topography-preserving tract filtering algorithms to successfully reconstruct the 23 fiber bundles for each subject, which were then used to calculate the probabilistic atlases in the MNI152 space for public release. In our

Publisher's Disclaimer: This is a PDF file of an unedited manuscript that has been accepted for publication. As a service to our customers we are providing this early version of the manuscript. The manuscript will undergo copyediting, typesetting, and review of the resulting proof before it is published in its final citable form. Please note that during the production process errors may be discovered which could affect the content, and all legal disclaimers that apply to the journal pertain.

^{**}Corresponding author: Yonggang Shi, Ph.D. Address: 2025 Zonal Ave. Los Angeles, CA 90033, USA. yshi@loni.usc.edu; Tel: 323-442-7246.

^{*}Y. Tang and W. Sun contributed equally to this work.

experimental results, we demonstrate that our method yielded anatomically faithful reconstruction of the brainstem pathways and achieved improved performance in comparison with an existing atlas of cerebellar peduncles based on HCP data. These atlases have been publicly released on NITRIC (https://www.nitrc.org/projects/brainstem_atlas/) and can be readily used by brain imaging researchers interested in studying brainstem pathways.

Keywords

Brainstem; Connectome; Pathways; Atlas; Tractography

Introduction

The brainstem plays a central role in efferent and afferent connections among the cerebral cortex, spinal cord and the cerebellum (Carpenter, 1976). Within this small and compact structure, the multitude of neuronal cell bodies in brainstem and their processes also comprise complex networks. From a connectome point of view, the brainstem is the site of origin, termination or relay center of many ascending and descending pathways (Standring, 2016). Fiber pathways in the brainstem are essential for sensory and motor functions, and they are known to be affected in a wide spectrum of neurological disorders such as the Alzheimer's disease (AD), Parkinson's disease (PD), multiple sclerosis, amyotrophic lateral sclerosis, hearing loss and sleep disorders (Delano-Wood et al., 2015; Grinberg et al., 2011; Jack et al., 2013; Jones and Pons, 1998; Simic et al., 2009). In particular, the recently updated Braak stages of AD (Braak et al., 2011) indicate that tau pathology in the locus coeruleus (LC) of the brainstem is an early event and propagation can occur to the transentorhinal cortex (Braak and Del Tredici, 2011). It has also been reported that LC degenerates progressively with AD severity (Theofilas et al., 2017). Damage to the brainstem is often devastating and life-threatening because it is a structurally and functionally compact region, where even small lesions can destroy centers vital for arousal or autonomic functions, disconnect forebrain motor areas from brainstem and spinal motor neurons, or sever incoming sensory fibers from higher centers of consciousness, perception and cognition (Lucey, 2016; Parraga et al., 2016; Sala et al., 2007; Yagmurlu et al., 2014). Therefore, the brainstem is often regarded as a restricted zone in neurosurgery.

Compared with the extensive use of diffusion MRI in studying the white matter connectivity of the forebrain (Catani and Thiebaut de Schotten, 2012; Mori et al., 2004), there has been limited research on the *in vivo* mapping of brainstem connectomes. Previous research based on cytoarchitecture studies have laid a great foundation by providing many detailed characterizations of brain stem nuclei in many highly valuable atlases (Büttner-Ennever et al., 2014; Haines, 2014; John Nolte, 2013; Paxinos et al., 2012; Paxinos, 1995). Current brain anatomy research focuses on mapping the pathways of brainstem nuclei such as the locus coeruleus, where challenges remain even in animal studies(Schwarz and Luo, 2015). For diffusion MRI studies, the focus is thus mostly on well-known motor, sensory, and cerebellar peduncles in brainstem. For the 3D modeling of brainstem pathways, diffusion MRI were successfully applied to postmortem brainstem samples for the reconstruction of major pathways (Aggarwal et al., 2013; Calabrese et al., 2015; Ford et al., 2013), but such

methods require long scanning times and are not practical for *in vivo* studies. While it is feasible to study some of the major brainstem bundles with conventional diffusion MRI (Alvarez-Linera, 2010; Chen et al., 2007; Salamon et al., 2005; Stieltjes et al., 2001; Wakana et al., 2007), the limited resolution and image quality have made a large-scale comprehensive investigation of human brainstem pathways challenging.

With multiband and other advanced MRI techniques such as multi-shell imaging, the Human Connectome Project (HCP) has developed MRI protocols to acquire multi-shell diffusion MRI (dMRI) for connectome studies at a resolution that is almost an order of magnitude higher than conventional approaches (Van Essen et al., 2012). Using the high-resolution HCP data, an atlas of brainstem bundles was recently proposed (Meola et al., 2016b), but this study only computed bundles on an average dataset of 488 HCP subjects, so individual variability was not represented. More importantly, all subjects were treated equally in this study without considering the widely present susceptibility-induced distortion artifacts of HCP data in the brainstem region, which we will discuss in more detail in the method section, thus potentially compromising the quality of the data used for atlas construction. In a related study, the HCP data of 90 subjects were used to construct a probabilistic atlas of cerebellar peduncles (van Baarsen et al., 2016). This atlas overcomes some limitation of previous cerebellar white matter atlases (Varentsova et al., 2014) such as the successful representation of the fiber crossings of the superior cerebellar peduncle. This work, however, did not consider the variable distortion artifacts in HCP data either and all subjects were included in atlas construction without quality control on the brainstem area of these datasets. Furthermore, another limitation of this study is that only ROIs delineated in the MNI152 atlas image were used for bundle reconstruction in individual subjects. For studying the ascending reticular activating system (ARAS), connectome imaging techniques were also applied to explore fiber pathways between brainstem and forebrain regions (Edlow et al., 2015; Edlow et al., 2012).

In this work, we develop and publicly distribute a novel probabilistic atlas of 23 brainstem pathways using HCP data of the highest quality with minimal distortion artifacts in the brainstem area (Figure 1). Compared with previous atlases on brainstem pathways, our work has the following novel contributions: First, we conduct extensive quality control on the connectome imaging data of 488 HCP subjects with complete diffusion MRI scans from the HCP-500 release to exclude datasets with significant distortion in the brainstem area. This is a critical issue as more than 80% of the HCP subjects have severe distortions in the brainstem area even after the application of the correction procedures from the HCP-Pipeline (Glasser et al., 2013). This quality control allows us to fully leverage the high-resolution HCP data for brainstem research without being compromised by the distortion artifacts in this area (Figure 1(A) and (B)). Second, we use our novel connectome modeling techniques including fiber orientation distribution (FOD) reconstruction from multi-shell imaging data (Tran and Shi, 2015) (Figure 1(A) and (B)) and tract filtering based on topographic regularity (Wang et al., 2017) for fiber bundle reconstruction. Third, we manually delineate ROIs on each subject using the high-resolution tract density images (TDI) (Calamante et al., 2010a) derived from FOD-based tractography to ensure the accurate placement of white matter boundaries for bundle reconstruction (Figure 1(C)). In total 1300 ROIs were manually delineated on 20 HCP subjects with reference to stained histology sections for the

reconstruction of brainstem bundles. Compared with previous works using HCP data that only labeled ROIs on one image, our efforts can provide more accurate delineation of bundle boundaries. We demonstrate in our experimental results that our method can generate high-quality and anatomically faithful reconstruction of brainstem pathways (Figure 1(D)). Using the fiber bundles from the 20 HCP subjects, we computed the probabilistic atlases of 23 brainstem bundles in the standard MNI152 space. These atlases have been publicly released on the NITRIC (https://www.nitrc.org/projects/brainstem_atlas/) and are included in the supplement.

Materials and Methods

MRI Data

T1-weighted 3D structural MRI and multi-shell diffusion MRI (dMRI) data of 488 subjects (289 females, 199 males; age=29.15±3.47 (mean±SD) years) with complete diffusion imaging data from the 500-Subject release of HCP were used in this study. The data were acquired in a modified Siemens 3T Skyra scanner with a customized protocol (Sotiropoulos et al., 2013). The T1-weighted MRI has an isotropic spatial resolution of 0.7mm, and the dMRI data has an isotropic spatial resolution of 1.25mm. The multi-shell dMRI data were collected over 270 gradient directions distributed over three b-values (1000, 2000, 3000 s/mm²). For each subject, the multi-shell dMRI data were collected with both L/R and R/L phase encodings using the same gradient table, which were then merged into a single copy of multi-shell dMRI data after the correction of distortions with the HCP Preprocessing Pipeline (Glasser et al., 2013).

FOD Computation from Multi-Shell Imaging

FODs were computed at each voxel to provide a probabilistic representation of the fiber direction. Here we utilized a novel FOD algorithm we developed recently for multi-shell imaging data (Tran and Shi, 2015). In this algorithm, the diffusion imaging signals at each voxel are modeled as composed of contributions from diffusion in the intra-axonal compartment, extra-axonal compartment and the DOT model (Panagiotaki et al., 2012) with negligible diffusion. The compartment modeling allows the robust reconstruction of FODs from multi-shell imaging data and the reconstruction of challenging brain pathways such as the Meyer's loop in the optic radiation (Kammen et al., 2016). As an illustration, we show in Figure 2 the reconstructed FODs in various brainstem areas of an HCP subject, which demonstrates that the FODs computed from the high-resolution HCP data provide very detailed characterizations of the fiber pathways in the brainstem.

Computation of Tract Density Imaging (TDI) Data

TDI provides an opportunity to gain high spatial resolution of white matter image using a post-processing approach based on fiber tractography (Calamante et al., 2010b). With TDI data, the anatomical contrast of brain white matter is enhanced for further analysis. Using the FODs generated by our algorithm, we ran whole brain tractography using a probabilistic tractography tool in MRTrix (Tournier et al., 2007) to generate 20 million fiber tracts for producing TDI data (Figure 3). For each subject, the TDI image was then calculated at an isotropic spatial resolution of 0.5mm and represented as a directionally-encoded color

(DEC) map to incorporate fiber directionality information. The colored TDI map facilitates the manual annotation of white matter ROIs because of its high anatomical contrast and encoded directionality information.

Quality Evaluation of Susceptibility Distortion Correction and Subject Selection

The dMRI data from HCP were acquired using echo planar imaging (EPI) technique, which is an efficient acquisition approach with high signal-to-noise ratio (SNR). However, the susceptibility of the magnetic field to the boundary between different tissues leads to geometrical distortions along the phase encoding (PE) direction. To tackle this problem, the HCP acquired dMRI data from two opposite PE directions (Andersson et al., 2003; Holland et al., 2010) and merged them into one corrected dataset using the estimated deformation fields from opposite PEs (Andersson et al., 2016), which is the preprocessed data released by HCP. Due to the tissue/air boundary around the brainstem region, however, the distortions of brainstem are usually more severe than other brain regions. Consequently, the residual distortions contained in the preprocessed HCP data can still severely compromise the analysis of brainstem fiber pathways. This can be clearly seen from the two examples shown in Figure 3, where we can see the brainstem structures are very disorganized in mid-pons for the unsatisfactory case. To further identify the root of the problem, we computed the FODs in a brainstem area of an HCP subject using data of each PE after distortion correction (Figure 4 (C) and (D)) but before they were merged, which will be the final output of the HCP-Pipeline. As shown in Figure 4 (E) and (F), we can clearly see the brainstem anatomy is severely misaligned even though the "corrected" B0 images appear undistorted in Figure 4 (C) and (D). Therefore, it is unlikely we will have a reliable estimation of fiber orientations with data generated by merging these preprocessed data from each PE. This is because the B0 image does not have enough contrast to resolve the complex brainstem anatomy and hence is an inherent challenge for studying brainstem connectomes with the HCP data.

To ensure only subjects with high quality data were used for brainstem bundle reconstruction, we screened data from all 488 subjects by visually inspecting the quality of their TDI and T1-weighted MRI. In total, only 70 of the 488 subjects were determined to have relatively good image quality. After exclusion of family members and careful consideration of gender balances, we selected 20 HCP subjects (10 males and 10 females) with high quality connectome imaging data for our atlas construction. Demographic details of the subjects used in this study have been included in the supplementary materials.

Fiber Bundles Included in the Atlas

The brainstem is rather compact both structurally and functionally with many small fiber pathways carrying cortical and spinal projections from nuclei within the brainstem. Even with the connectome imaging techniques, it is unrealistic to label and reconstruct all the fiber tracts in the brainstem *in vivo*. In this work, we reconstruct 23 major brainstem fiber bundles (Table 1) from the cohort of 20 HCP subjects with high quality connectome imaging data. We choose those bundles in our atlas for the following reasons. First, these bundles are structurally and functionally well-characterized in brain anatomy. Second, critical sections of the bundles can be clearly identified on the TDI or structural MRIs, which allows for the reliable delineation of anatomical ROIs for tractography-based reconstruction. Third, once

reconstructed, these major bundles can serve as reference landmarks for the segmentation of other structures within the brainstem. Overall these 23 brainstem bundles can be divided into three groups: 1) Major motor tracts running principally on the ventral surface of the brainstem: the corticospinal tract (CST), the fronto-pontine tract (FPT), and the parieto-occipito-temporo-pontine tract (POTPT); 2) Major sensory tracts including the medial lemniscus (ML), the spinothalamic tract (STT), and the lateral lemniscus (LL); 3) Cerebellar peduncles that include the superior cerebellar peduncle (SCP), the middle cerebellar peduncle (MCP), and the inferior cerebellar peduncle (ICP). More specifically, the SCP is mainly composed of the anterior spinocerebellar tract (SCPSC), the cerebellorubral tract (SCPCR), and the cerebellothalamic tract (SCPCT). The ICP mainly consists of afferent tracts from the medulla oblongata to the cerebellum (ICPMCT) (i.e., restiform body) and the vestibulocerebellar tract (ICPVCT). Instead of treating the SCP and ICP as single bundle, which was typical in previous works, we reconstruct these individual components in our project. This in turn provides a more fine-grained atlas for these cerebellar pathways.

ROI-based Bundle Reconstruction

Following previous works on fiber bundle reconstruction (Catani and Thiebaut de Schotten, 2012; Oishi et al., 2009), we adopted an ROI-based approach for brainstem bundle reconstruction. Several detailed atlases of stained histological sections (Nolte, 2008, 2013; Paxinos et al., 2012) and the well-known brainstem anatomy (Standring, 2016) were referenced for the definition of the 23 white matter tracts within the brainstem. Most of the labels were annotated on the TDI data, which can provide high spatial resolution and clear anatomical contrast of white matter regions. For gray matter regions such as the inferior colliculus (Figure 5 (G) and (H)), we labeled them on the co-registered T1-weighted MRI from the HCP Preprocessing Pipeline (Glasser et al., 2013). We also used automatically segmented brain regions including the thalamus and cerebellum from FreeSurfer (Fischl, 2012) for bundle reconstruction.

Manual ROI delineation was performed by an experienced anatomist (Y. Tang) and reviewed by two other team members with experience in brain anatomy and bundle reconstruction (J. Ringman and Y Shi). The delineation process was performed using the ITK-SNAP software (Yushkevich et al., 2006). For each fiber bundle, we developed a delineation protocol with a set of inclusion ROIs that the bundle must touch. In addition, we also included start and end ROIs for certain bundles where a clear anatomical definition was available. Whenever possible, we used stained histological sections at comparable brainstem locations as reference for the delineation on the TDI image. As a demonstration, we show in Figure 5 (A)–(F) the side-by-side comparisons of ROIs on histology and TDI sections at the midbrain, pons, and the medulla oblongata. For each bundle, we denote an ROI using a combination of bundle name, the hemisphere, and its order in all ROIs of the bundle. For example, the *x*-th ROI of the CST bundle on the left and right hemisphere are named as *CST_Lx* and *CST_Rx*, respectively. A detailed description of the delineation protocol and ROIs for all bundles are included in the supplemental material.

A summary of the reconstruction protocol using FOD-based tractography is listed in Table 1. For each bundle, the ROIs are listed in the order through which a fiber tract should pass.

When an ROI is used as the starting point of the bundle, we color it as green. For ROIs used as the end point of a bundle, we color them as red. In particular, we want to mention that the MCP is reconstructed as the combination of three bundles to capture fiber tracts from the pontine nuclei to the cerebellum (1. Fiber tracts from pontine nuclei to the left cerebellum; 2. Fiber tracts from pontine nuclei to the right cerebellum; 3. Fiber tracts successfully traversing the whole trajectory from the left to right cerebellum). Following the ROI-based protocols in Table 1, we run the probabilistic tractography tool in MRTrix (Tournier et al., 2007) based on the FODs computed by our novel algorithm for multi-shell imaging. The same tractography parameters: $step_size = 0.125$ mm, $angle = 4^{\circ}$, and $cutoff_threshold = 0.025$ were used for all bundles. After a bundle is computed with FOD-based tractography, we applied a novel tract filtering algorithm based on topographic regularity (Wang et al., 2017) to remove outlier tracts and obtain the final bundle for atlas construction.

Probabilistic Atlas Construction

Using the ANTS software (Avants et al., 2008), a nonlinear warp was first computed to register the T1-weighted MRI of each HCP subject to the MNI152 space. Given a reconstructed brainstem bundle, we first computed its TDI and normalized it with its maximum intensity, which created a fraction map with intensities between 0 and 1. The fraction maps of the same bundle from all subjects were then warped to the MNI152 space using the nonlinear warp computed by ANTS. The warped fraction maps were finally summed together and divided by the number of subjects to obtain the probabilistic atlas of this bundle. This process was repeated for all bundles to create the probabilistic atlas of 23 brainstem bundles in the MNI152 space (Supplemental Material).

Results

Main Brainstem Pathways from HCP Subjects

Following the protocols in Table 1, we successfully reconstructed the 23 brainstem bundles in all 20 HCP subjects. The reconstructed bundles from three representative subjects are shown in Figure 6 from the frontal and lateral views. Main bundles have been plotted with distinct colors and annotated with different numbers for their easy identification. These results provide an overview of the brainstem connectomes formed by these major bundles, and their topographic arrangements within the brainstem.

To more clearly present the trajectories of the reconstructed fiber bundles, we divide them into three groups and show the results from the same three subjects in Figure 7. The first group of tracts consist of the major motor tracts (FPT, CST, and POTPT) from both hemispheres. All three tracts originate from the cerebral cortex and pass through the internal capsule to reach the brainstem. We only reconstruct these tracts after they enter the brainstem at the cerebral peduncle. As shown in Figure 7 (A)-(C), they are principally located along the ventral surface of the brainstem. Both the FPT and POPPT terminate at the pontine nuclei, and the CST continues along the pyramid part of the medulla oblongata. The second group of tracts include the bilateral sensory tracts (ML, STT, LL) and are shown in Figure 7 (D)-(E). We can see that they pass through the dorsal area of the pons and are located posteriorly to the motor tracts. As the ML and STT travel from the medulla

oblongata toward the midbrain, the STT maintains a posterolateral position with respect to the ML in both the pons and midbrain. Both the ML and STT project to the ventral posterolateral (VPL) nucleus of the thalamus. The LL terminates at the inferior colliculus. The third group of tracts from the cerebellar peduncles (SCP, MCP and ICP) are shown in Figure 7 (F)-(H). For the SCP, we only show the SCPCT component to demonstrate that our method successfully captured their crossing around the red nucleus on their way from the cerebellum to the thalamus on the opposite hemisphere. The SCP from the left and right cerebellar hemisphere are colored in blue and red, respectively. We show the MCP as a single bundle and color it as cyan. The MCP mostly connects the pontine nuclei to the opposite hemisphere of the cerebellum, and is located lateral to both the SCP and ICP in the cerebellum as clearly demonstrated in our reconstruction results. For the ICP, we merge the ICPMCT and ICPVCT components on each hemisphere for this visualization. The ICPMCT is an afferent compact fiber tract composed of the posterior spinocerebellar fibers and the trigeminocerebellar, cuneocerebellar, reticulocerebellar and olivocerebellar tracts from the medulla oblongata. The ICPVCT starts from the vestibular nucleus, travels through the pontine tegmentum and ends in the cerebellar cortex. The left and right ICP are plotted as yellow and green, respectively.

Some projection of brainstem bundles to the thalamus have been described in neuroanatomy. To further illustrate the high-quality reconstruction achieved by our method, we plotted in Figure 8 the projection of the SCP, ML, and STT onto the thalamic surfaces and show that they are consistent with descriptions in brain anatomy (Haines, 2013; Standring, 2016). We can clearly see that the SCP bundles project to the ventrolateral and anterior nuclei of the thalamus on the opposite hemisphere. For ML and STT, they both project to the ventral posterolateral (VPL) nuclei of the thalamus on the same hemisphere.

Probabilistic Atlas of Brainstem Bundles in the MNI152 Space

Using the reconstruction results from all 20 HCP subjects, we have computed the probabilistic atlas for each of the 23 brainstem bundles in the MNI152 space. The NIFTI file of the 23 atlases are included in the supplemental material and have been publicly distributed on the NITRC website (https://www.nitrc.org/projects/brainstem_atlas/). In Figure 9, we present a snapshot of the atlases of the 23 bundles. For each bundle except the MCP, we plotted the left and right tracts in blue and red, respectively, on a representative axial, coronal, and sagittal slice. On the left column of Figure 9, we plotted the atlases of motor and sensory tracts. Tracts from the cerebellar peduncles were plotted in the right column of Figure 9. The SCPCT and SCPCR include the efferent fibers of SCP and their crossings have been clearly captured and shown on the axial slices. The SCPSC represents the afferent tracts of SCP, most prominently the anterior spinocerebellar tract. The atlas of two ICP components (ICPMCT and ICPVCT) are also plotted on the lower right corner of Figure 9. While they exhibit similar appearances because their fiber tracts do follow a closely attached trajectory, the VN component (ICPVCT) can still be observed to occupy a slightly more posterior position.

To quantify the variability of individual subjects with respect to the probabilistic atlas, we calculated the pairwise overlap of warped tracts among the 20 HCP subjects in the MNI152

space. By thresholding each bundle atlas at a given probability level, we generated a mask and computed the pairwise Dice overlap coefficient among the 20 subjects within this mask. For every bundle, 190 pairwise Dice coefficients were thus computed at each probability level. At the probability level of 10% and 30%, box plots of the Dice coefficients of each bundle are shown in Figure 10 (A) and (B), respectively. With the increase of the probability level from 10% to 30%, we can see that the overlap of the warped tracts also increases to a higher level (>0.9). Due to the sparse fiber tracts of the SCP and ICP bundles in the cerebellum region, we observe relatively higher variability in these two bundles as compared to the motor and sensory tracts.

Comparison with a Previous Atlas of Cerebellar Peduncles

Besides the motor and sensory tracts that are contained within the brainstem, our atlases included cerebellar peduncles reconstructed using the HCP data. It is thus desirable to compare with the previous atlas of cerebellar peduncles also constructed from HCP data (van Baarsen et al., 2016). The main distinction of our work is that we have more detailed ROI controls on each subject. We have also reconstructed individual components of SCP and ICP, while the previous atlas treated them as a single bundle. As a demonstration, we plotted in Figure 11 the atlas of the left SCP bundle that projects to the right thalamus from both atlases. We can see in general both atlases follow a similar trajectory when the SCP travels from the brainstem toward the thalamus. The main difference is that our atlas does not include the spurious branch contained in the previous atlas. This is because we included ROIs around the red nucleus in our SCPCT protocol (Table 1).

Discussion

In our research, 23 brainstem fiber bundles were reconstructed, which can be divided into three groups according to their pathways and functional properties. The motor tracts including the CST, FPT and POTPT occupy the basal lamina (cerebral peduncle in midbrain, basal portion in pons and pyramid in medulla). The major sensory tracts including the ML, STT, LL are in the tegmentum with a relatively stable topographic relationship. As demonstrated in Figure 6-8, our reconstruction results match well with neuroanatomy described in previous literature and postmortem studies with histological staining. The atlas of brainstem bundles from this work will facilitate the study of brainstem structure and functions in neuroimaging research of various neurological disorders and can also be of value for neurosurgical planning.

While tractography techniques have been successfully applied for the reconstruction of major fiber bundles in the forebrain (Ahn and Lee, 2011; Auriat et al., 2015; Basser et al., 2000; Berman et al., 2005; Zhang et al., 2010), their application in the compact brainstem area has been more challenging. The complex anatomy and the usually severe distortion artifacts of the imaging data in the brainstem area are two main difficulties for studying the brainstem connectome. In this work, we leverage the high resolution, multi-shell diffusion imaging data of HCP from two phase encodings to develop a novel atlas of human brainstem pathways. An important strength of our work is that we devoted systematic effort to visually inspect the quality of 488 HCP datasets for the selection of a set of 20 unrelated subjects (10

males, 10 females) with minimal residual distortions from susceptibility. Following well-established neuroanatomy, we manually delineate a suite of carefully selected ROIs for the 23 fiber bundles on each of the 20 brain images. Cutting-edge FOD-based tractography and topography-preserving filtering algorithms were then applied to reconstruct the fiber bundles. With the successfully reconstructed bundles from the 20 HCP subjects, we have built the probabilistic atlases of the 23 brainstem bundles in the MNI152 space for public distribution.

Compared with previous efforts on studying the brainstem connectomes using HCP data (Meola et al., 2016a; Meola et al., 2016b; van Baarsen et al., 2016), our work has the following unique aspects. First, we carefully examined the distortion artifacts of preprocessed HCP data in the brainstem area and only used data with minimal distortion in our atlas construction. This is critical as we found that more than 80% of the preprocessed HCP data has severe distortions in the brainstem area. No such quality control was conducted in previous works and more than likely these low-quality data were included for studying brainstem connectivity. Second, we performed ROI delineation on individual subjects instead of only in the atlas space. With the high-resolution TDIs, we were able to extract accurate white matter boundaries to serve as key ROIs for constraining the trajectories of fiber bundles such as the SCP_L1 and SCP_R1 ROIS described in the supplemental material. In previous studies, either the SCP or the ICP was constructed as one tract (van Baarsen et al., 2016) even though anatomically they are both composed of several sub-tracts according to the neuroanatomy (Standring, 2016). In our work, we developed a more refined protocol for both the SCP and ICP to reconstruct their individual components. Our detailed ROI protocol also removes possible outliers in a previous atlas as shown in Figure 11. Third, we used our cutting-edge algorithm for FOD reconstruction from multishell imaging data and novel tract filtering algorithm for removing outliers from reconstructed bundles. These novel techniques allow the robust reconstruction of crossing fibers from bundles such as the SCP. Overall, these concerted efforts lead to the successful reconstruction of 23 brainstem bundles for atlas construction.

One limitation of our work is that we only focused on the main motor and sensory tracts, and cerebellar peduncles. This choice is based on their relatively well-described anatomy. There is a need of considerable future work to reconstruct pathways from other brainstem nuclei. For example, the brainstem includes a complex network of gray matter and white matter, known as the reticular formation, that is not only vital for the regulation of cardiac, respiratory, muscle and reflex activities, but also important for cerebral arousal and the maintenance of consciousness. Our atlas currently did not include fiber tracts from the raphe nuclei of the reticular formation, which are receiving increasing attention, for example in relation to their involvement in the tau pathology of Alzheimer's disease and related dementias. The trajectories of the fiber tracts from the raphe nuclei, however, are less wellcharacterized. Advances in tracer injection studies hold the promise of providing increasing amount of knowledge about these challenging pathways (Oh et al., 2014; Zingg et al., 2014). The delineation of raphe nuclei on current MRI scans is also challenging due to the lack of contrast. Special pulse sequences for highlighting neuromelanin could be valuable for delineating the locus coeruleus, but they are not always available. Fortunately, the main bundles reconstructed in our study have often been used as references for describing the

location of the raphe nuclei, so the current atlas can be viewed as a steppingstone toward mapping the fiber pathways from the raphe and other brainstem nuclei. The use of only young and healthy subjects from HCP could be another limitation of our atlas. With advanced nonlinear image registration techniques such as the ANTS software, however, we anticipate our atlas could be applied to a wide range of studies similar to the MNI152 atlas. With the emergence of connectome data from the LifeSpan connectome project and other disease-related connectome projects, we can also apply the same protocol to create customized atlases for specific age and disease groups.

In summary, the main contribution of this work is the creation of a probabilistic atlas of 23 main brainstem bundles using high-quality connectome imaging data and advanced analysis techniques. We have publicly distributed this atlas on the NITRC website and included it in the supplement material of this paper. Our atlas can be valuable in brain imaging studies of various neurological disorders such as the Alzheimer's disease (AD), Parkinson's disease (PD), and multiple sclerosis. It can also serve as a basis for the segmentation of other brainstem structures according to their topographic arrangements. For future work, we will develop automated approaches for the reconstruction of brainstem bundles and study their application in large-scale connectome research. We will also investigate the reconstruction of other fiber bundles such as those from the raphe and other brainstem nuclei and their application in studying brain disorders.

Supplementary Material

Refer to Web version on PubMed Central for supplementary material.

Acknowledgments

This work was in part supported by the National Institute of Health (NIH) under Grant R01EB022744, U01AG051218, U01EY025864, P41EB015922, P50AG05142, R01AG025340. The work of Y Tang was also in part supported by the National Natural Science Foundation of China through the NSFC Roadmap FPR Basic Medical Research (Grant number: 81301280) and China Scholarship Council (No. 201506225068). Data used in this paper were provided by the Human Connectome Project, WU-Minn Consortium (Principal Investigators: David Van Essen and Kamil Ugurbil; 1U54MH091657) funded by the 16 NIH Institutes and Centers that support the NIH Blueprint for Neuroscience Research; and by the McDonnell Center for Systems Neuroscience at Washington University.

References

- Aggarwal M, Zhang J, Pletnikova O, Crain B, Troncoso J, Mori S. Feasibility of creating a high-resolution 3D diffusion tensor imaging based atlas of the human brainstem: a case study at 11.7 T. Neuroimage. 2013; 74:117–127. [PubMed: 23384518]
- Ahn S, Lee SK. Diffusion tensor imaging: exploring the motor networks and clinical applications. Korean J Radiol. 2011; 12:651–661. [PubMed: 22043146]
- Alvarez-Linera J. Magnetic resonance techniques for the brainstem. Semin Ultrasound CT MR. 2010; 31:230–245. [PubMed: 20483391]
- Andersson JL, Graham MS, Zsoldos E, Sotiropoulos SN. Incorporating outlier detection and replacement into a non-parametric framework for movement and distortion correction of diffusion MR images. Neuroimage. 2016
- Andersson JLR, Skare S, Ashburner J. How to correct susceptibility distortions in spin-echo echoplanar images: application to diffusion tensor imaging. Neuroimage. 2003; 20:870–888. [PubMed: 14568458]

Auriat AM, Borich MR, Snow NJ, Wadden KP, Boyd LA. Comparing a diffusion tensor and non-tensor approach to white matter fiber tractography in chronic stroke. Neuroimage Clin. 2015; 7:771–781. [PubMed: 25844329]

- Avants BB, Epstein CL, Grossman M, Gee JC. Symmetric diffeomorphic image registration with cross-correlation: evaluating automated labeling of elderly and neurodegenerative brain. Med Image Anal. 2008; 12:26–41. [PubMed: 17659998]
- Basser PJ, Pajevic S, Pierpaoli C, Duda J, Aldroubi A. In vivo fiber tractography using DT-MRI data. Magn Reson Med. 2000; 44:625–632. [PubMed: 11025519]
- Berman JI, Mukherjee P, Partridge SC, Miller SP, Ferriero DM, Barkovich AJ, Vigneron DB, Henry RG. Quantitative diffusion tensor MRI fiber tractography of sensorimotor white matter development in premature infants. Neuroimage. 2005; 27:862–871. [PubMed: 15978841]
- Braak H, Del Tredici K. Alzheimer's pathogenesis: is there neuron-to-neuron propagation? Acta Neuropathol. 2011; 121:589–595. [PubMed: 21516512]
- Braak H, Thal DR, Ghebremedhin E, Del Tredici K. Stages of the pathologic process in Alzheimer disease: age categories from 1 to 100 years. J Neuropathol Exp Neurol. 2011; 70:960–969. [PubMed: 22002422]
- Büttner-Ennever, JA., Horn, AKE., Olszewski, J. Olszewski and Baxter's Cytoarchitecture of the human brainstem. Karger, Basel; New York: 2014. 3rd, revised and extended edition ed
- Calabrese E, Hickey P, Hulette C, Zhang J, Parente B, Lad SP, Johnson GA. Postmortem diffusion MRI of the human brainstem and thalamus for deep brain stimulator electrode localization. Hum Brain Mapp. 2015; 36:3167–3178. [PubMed: 26043869]
- Calamante F, Tournier JD, Jackson GD, Connelly A. Track-density imaging (TDI): Super-resolution white matter imaging using whole-brain track-density mapping. Neuroimage. 2010a; 53:1233–1243. [PubMed: 20643215]
- Calamante F, Tournier JD, Jackson GD, Connelly A. Track-density imaging (TDI): super-resolution white matter imaging using whole-brain track-density mapping. Neuroimage. 2010b; 53:1233–1243. [PubMed: 20643215]
- Carpenter, MB. Human Neuroanatomy. The Williams and Wilkins Company; 1976.
- Catani, M., Thiebaut de Schotten, M. Atlas of Human Brain Connections. Oxford University Press (OUP); 2012.
- Chen X, Weigel D, Ganslandt O, Buchfelder M, Nimsky C. Diffusion tensor imaging and white matter tractography in patients with brainstem lesions. Acta Neurochir (Wien). 2007; 149:1117–1131. discussion 1131. [PubMed: 17712509]
- Delano-Wood L, Bangen KJ, Sorg SF, Clark AL, Schiehser DM, Luc N, Bondi MW, Werhane M, Kim RT, Bigler ED. Brainstem white matter integrity is related to loss of consciousness and postconcussive symptomatology in veterans with chronic mild to moderate traumatic brain injury. Brain Imaging Behav. 2015; 9:500–512. [PubMed: 26248618]
- Edlow BL, McNab JA, Witzel T, Kinney HC. The Structural Connectome of the Human Central Homeostatic Network. Brain Connect. 2015; 6:187–200. [PubMed: 26530629]
- Edlow BL, Takahashi E, Wu O, Benner T, Dai G, Bu L, Grant PE, Greer DM, Greenberg SM, Kinney HC, Folkerth RD. Neuroanatomic connectivity of the human ascending arousal system critical to consciousness and its disorders. J Neuropathol Exp Neurol. 2012; 71:531–546. [PubMed: 22592840]
- Fischl B. FreeSurfer. Neuroimage. 2012; 62:774–781. [PubMed: 22248573]
- Ford AA, Colon-Perez L, Triplett WT, Gullett JM, Mareci TH, Fitzgerald DB. Imaging white matter in human brainstem. Front Hum Neurosci. 2013; 7:400. [PubMed: 23898254]
- Glasser MF, Sotiropoulos SN, Wilson JA, Coalson TS, Fischl B, Andersson JL, Xu J, Jbabdi S, Webster M, Polimeni JR, Van Essen DC, Jenkinson M, Consortium, W.U.-M.H. The minimal preprocessing pipelines for the Human Connectome Project. Neuroimage. 2013; 80:105–124. [PubMed: 23668970]
- Grinberg LT, Rueb U, Heinsen H. Brainstem: neglected locus in neurodegenerative diseases. Front Neurol. 2011; 2:42. [PubMed: 21808630]
- Haines, DE. Fundamental Neuroscience for Basic and Clinical Applications. Elsevier; Philadelphia: 2013.

Haines, DE. Neuroanatomy in Clinical Context: An Atlas of Structures, Sections, Systems, and Syndromes. 9th. Wolters Kluwer | Lippincott Williams & Wilkins; 2014.

- Holland D, Kuperman JM, Dale AM. Efficient correction of inhomogeneous static magnetic field-induced distortion in Echo Planar Imaging. Neuroimage. 2010; 50:175–183. [PubMed: 19944768]
- Jack CR Jr, Knopman DS, Jagust WJ, Petersen RC, Weiner MW, Aisen PS, Shaw LM, Vemuri P, Wiste HJ, Weigand SD, Lesnick TG, Pankratz VS, Donohue MC, Trojanowski JQ. Tracking pathophysiological processes in Alzheimer's disease: an updated hypothetical model of dynamic biomarkers. Lancet Neurol. 2013; 12:207–216. [PubMed: 23332364]
- John Nolte, JBA. Human Brain in Photographs and Diagrams. ELSEVIER; Philadelphia: 2013.
- Jones EG, Pons TP. Thalamic and brainstem contributions to large-scale plasticity of primate somatosensory cortex. Science. 1998; 282:1121–1125. [PubMed: 9804550]
- Kammen A, Law M, Tjan BS, Toga AW, Shi Y. Automated retinofugal visual pathway reconstruction with multi-shell HARDI and FOD-based analysis. Neuroimage. 2016; 125:767–779. [PubMed: 26551261]
- Lucey BP. The brainstem and traumatic brain injury. Science Translational Medicine. 2016; 8:344ec399.
- Meola A, Comert A, Yeh FC, Sivakanthan S, Fernandez-Miranda JC. The nondecussating pathway of the dentatorubrothalamic tract in humans: human connectome-based tractographic study and microdissection validation. J Neurosurg. 2016a; 124:1406–1412. [PubMed: 26452117]
- Meola A, Yeh FC, Fellows-Mayle W, Weed J, Fernandez-Miranda JC. Human Connectome-Based Tractographic Atlas of the Brainstem Connections and Surgical Approaches. Neurosurgery. 2016b; 79:437–455. [PubMed: 26914259]
- Mori, S., Wakana, S., Van Zijl, PCM. MRI atlas of human white matter. 1st. Elsevier; Amsterdam, The Netherlands; San Diego, CA: 2004.
- Nolte, J. The Human Brain: An Introduction to Its Functional Anatomy. 6. Mosby Elsevier; 2008.
- Nolte, J. The Human Brain in Photographs and Diagrams. 4. Saunders Elsevier; 2013.
- Oh SW, Harris JA, Ng L, Winslow B, Cain N, Mihalas S, Wang Q, Lau C, Kuan L, Henry AM, Mortrud MT, Ouellette B, Nguyen TN, Sorensen SA, Slaughterbeck CR, Wakeman W, Li Y, Feng D, Ho A, Nicholas E, Hirokawa KE, Bohn P, Joines KM, Peng H, Hawrylycz MJ, Phillips JW, Hohmann JG, Wohnoutka P, Gerfen CR, Koch C, Bernard A, Dang C, Jones AR, Zeng H. A mesoscale connectome of the mouse brain. Nature. 2014; 508:207–214. [PubMed: 24695228]
- Oishi K, Faria A, Jiang H, Li X, Akhter K, Zhang J, Hsu JT, Miller MI, van Zijl PC, Albert M, Lyketsos CG, Woods R, Toga AW, Pike GB, Rosa-Neto P, Evans A, Mazziotta J, Mori S. Atlasbased whole brain white matter analysis using large deformation diffeomorphic metric mapping: application to normal elderly and Alzheimer's disease participants. Neuroimage. 2009; 46:486–499. [PubMed: 19385016]
- Panagiotaki E, Schneider T, Siow B, Hall MG, Lythgoe MF, Alexander DC. Compartment models of the diffusion MR signal in brain white matter: A taxonomy and comparison. Neuroimage. 2012; 59:2241–2254. [PubMed: 22001791]
- Parraga RG, Possatti LL, Alves RV, Ribas GC, Ture U, de Oliveira E. Microsurgical anatomy and internal architecture of the brainstem in 3D images: surgical considerations. J Neurosurg. 2016; 124:1377–1395. [PubMed: 26517774]
- Paxinos, G., Huang, X., Sengul, G., Watson, C. Organization of brainstem nuclei The Human Nervous System. Elsevier Academic Press; 2012. p. 260-327.
- Paxinos, G., Huang, X. Atlas of Human Brainstem. Elsevier; 1995.
- Sala F, Manganotti P, Tramontano V, Bricolo A, Gerosa M. Monitoring of motor pathways during brain stem surgery: what we have achieved and what we still miss? Neurophysiol Clin. 2007; 37:399–406. [PubMed: 18083495]
- Salamon N, Sicotte N, Alger J, Shattuck D, Perlman S, Sinha U, Schultze-Haakh H, Salamon G. Analysis of the brain-stem white-matter tracts with diffusion tensor imaging. Neuroradiology. 2005; 47:895–902. [PubMed: 16158279]
- Schwarz LA, Luo L. Organization of the Locus Coeruleus-Norepinephrine System. Curr Biol. 2015; 25:R1051–1056. [PubMed: 26528750]

Simic G, Stanic G, Mladinov M, Jovanov-Milosevic N, Kostovic I, Hof PR. Does Alzheimer's disease begin in the brainstem? Neuropathol Appl Neurobiol. 2009; 35:532–554. [PubMed: 19682326]

- Sotiropoulos SN, Jbabdi S, Xu J, Andersson JL, Moeller S, Auerbach EJ, Glasser MF, Hernandez M, Sapiro G, Jenkinson M, Feinberg DA, Yacoub E, Lenglet C, Van Essen DC, Ugurbil K, Behrens TE, Consortium, W.U.-M.H. Advances in diffusion MRI acquisition and processing in the Human Connectome Project. Neuroimage. 2013; 80:125–143. [PubMed: 23702418]
- Standring, S. Gray's anatomy: the anatomical basis of clinical practice. Forty-first. Elsevier Limited; New York: 2016.
- Stieltjes B, Kaufmann WE, van Zijl PC, Fredericksen K, Pearlson GD, Solaiyappan M, Mori S. Diffusion tensor imaging and axonal tracking in the human brainstem. Neuroimage. 2001; 14:723–735. [PubMed: 11506544]
- Theofilas P, Ehrenberg AJ, Dunlop S, Di Lorenzo Alho AT, Nguy A, Leite REP, Rodriguez RD, Mejia MB, Suemoto CK, Ferretti-Rebustini REDL, Polichiso L, Nascimento CF, Seeley WW, Nitrini R, Pasqualucci CA, Jacob Filho W, Rueb U, Neuhaus J, Heinsen H, Grinberg LT. Locus coeruleus volume and cell population changes during Alzheimer's disease progression: A stereological study in human postmortem brains with potential implication for early-stage biomarker discovery. Alzheimer's & Dementia. 2017; 13:236–246.
- Tournier JD, Calamante F, Connelly A. Robust determination of the fibre orientation distribution in diffusion MRI: non-negativity constrained super-resolved spherical deconvolution. Neuroimage. 2007; 35:1459–1472. [PubMed: 17379540]
- Tran G, Shi Y. Fiber Orientation and Compartment Parameter Estimation from Multi-Shell Diffusion Imaging. IEEE Trans Med Imaging. 2015; 34:2320–2332. [PubMed: 25966471]
- van Baarsen KM, Kleinnijenhuis M, Jbabdi S, Sotiropoulos SN, Grotenhuis JA, van Cappellen van Walsum AM. A probabilistic atlas of the cerebellar white matter. Neuroimage. 2016; 124:724–732. [PubMed: 26385011]
- Van Essen DC, Ugurbil K, Auerbach E, Barch D, Behrens TE, Bucholz R, Chang A, Chen L, Corbetta M, Curtiss SW, Della Penna S, Feinberg D, Glasser MF, Harel N, Heath AC, Larson-Prior L, Marcus D, Michalareas G, Moeller S, Oostenveld R, Petersen SE, Prior F, Schlaggar BL, Smith SM, Snyder AZ, Xu J, Yacoub E, Consortium, W.U.-M.H. The Human Connectome Project: a data acquisition perspective. Neuroimage. 2012; 62:2222–2231. [PubMed: 22366334]
- Varentsova A, Zhang S, Arfanakis K. Development of a high angular resolution diffusion imaging human brain template. Neuroimage. 2014; 91:177–186. [PubMed: 24440528]
- Wakana S, Caprihan A, Panzenboeck MM, Fallon JH, Perry M, Gollub RL, Hua K, Zhang J, Jiang H, Dubey P, Blitz A, van Zijl P, Mori S. Reproducibility of quantitative tractography methods applied to cerebral white matter. Neuroimage. 2007; 36:630–644. [PubMed: 17481925]
- Wang, J., Aydogan, DB., Varma, R., Toga, AW., Shi, Y. Topographic Regularity for Tract Filtering in Brain Connectivity. In: Niethammer, M.Styner, M.Aylward, S.Zhu, H.Oguz, I.Yap, P-T., Shen, D., editors. Information Processing in Medical Imaging: 25th International Conference, IPMI 2017; Boone, NC, USA. June 25–30, 2017; Cham: Springer International Publishing; 2017. p. 263-274.Proceedings
- Yagmurlu K, Rhoton AL Jr, Tanriover N, Bennett JA. Three-dimensional microsurgical anatomy and the safe entry zones of the brainstem. Neurosurgery. 2014; 10(Suppl 4):602–619. discussion 619–620. [PubMed: 24983443]
- Yushkevich PA, Piven J, Hazlett HC, Smith RG, Ho S, Gee JC, Gerig G. User-guided 3D active contour segmentation of anatomical structures: significantly improved efficiency and reliability. Neuroimage. 2006; 31:1116–1128. [PubMed: 16545965]
- Zhang Y, Zhang J, Oishi K, Faria AV, Jiang H, Li X, Akhter K, Rosa-Neto P, Pike GB, Evans A, Toga AW, Woods R, Mazziotta JC, Miller MI, van Zijl PC, Mori S. Atlas-guided tract reconstruction for automated and comprehensive examination of the white matter anatomy. Neuroimage. 2010; 52:1289–1301. [PubMed: 20570617]
- Zingg B, Hintiryan H, Gou L, Song MY, Bay M, Bienkowski MS, Foster NN, Yamashita S, Bowman I, Toga AW, Dong HW. Neural networks of the mouse neocortex. Cell. 2014; 156:1096–1111. [PubMed: 24581503]

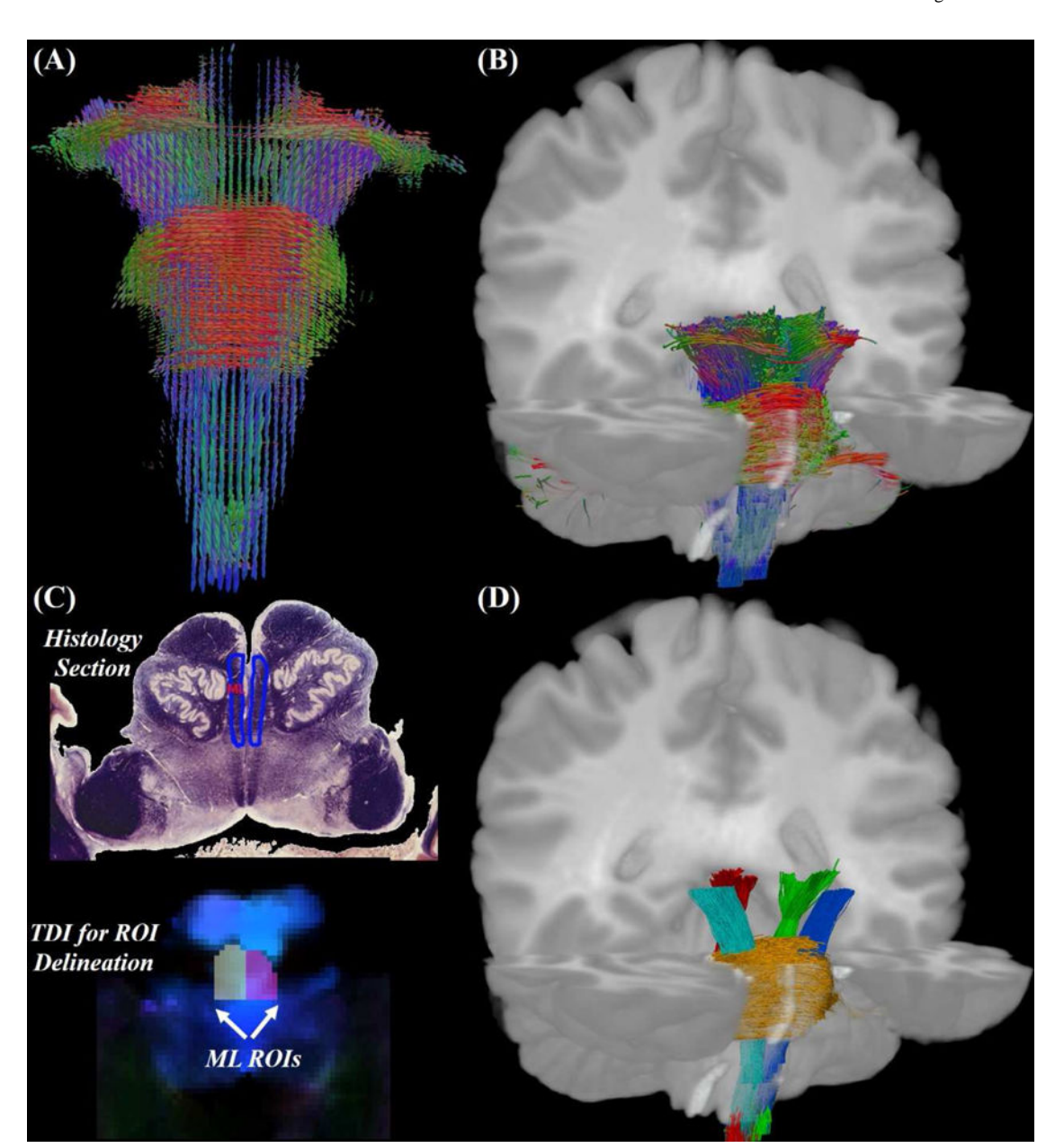


Figure 1.

An illustration of main processing techniques used in this work for brainstem pathway reconstruction from connectome imaging data. (A) FODs in the brainstem area computed from selected HCP data with minimal distortion artifacts. The FODs are rendered with the software Quantitative Imaging Toolkit (http://brayns.com/qitwiki). (B) With FOD-based tractography, digital representation of brainstem pathways can be computed. (C) Guided by stained histology sections (top, from Nolte's human brain atlas (Nolte, 2013) and reproduced with permission), we manually delineate ROIs on the tract density images (TDI) data derived from FOD-based tractography (bottom) for the extraction of specific fiber bundles. Here we use the medium lemniscus (ML) pathway as an example. (D) By applying our methods to the connectome imaging data, a rich set of 23 bundles will be reconstructed

in this work. As an illustration, we plot here the middle cerebellar peduncle (yellow), cortico-spinal tract (left: blue; right: cyan), and the medium lemniscus (left: green; right: red).

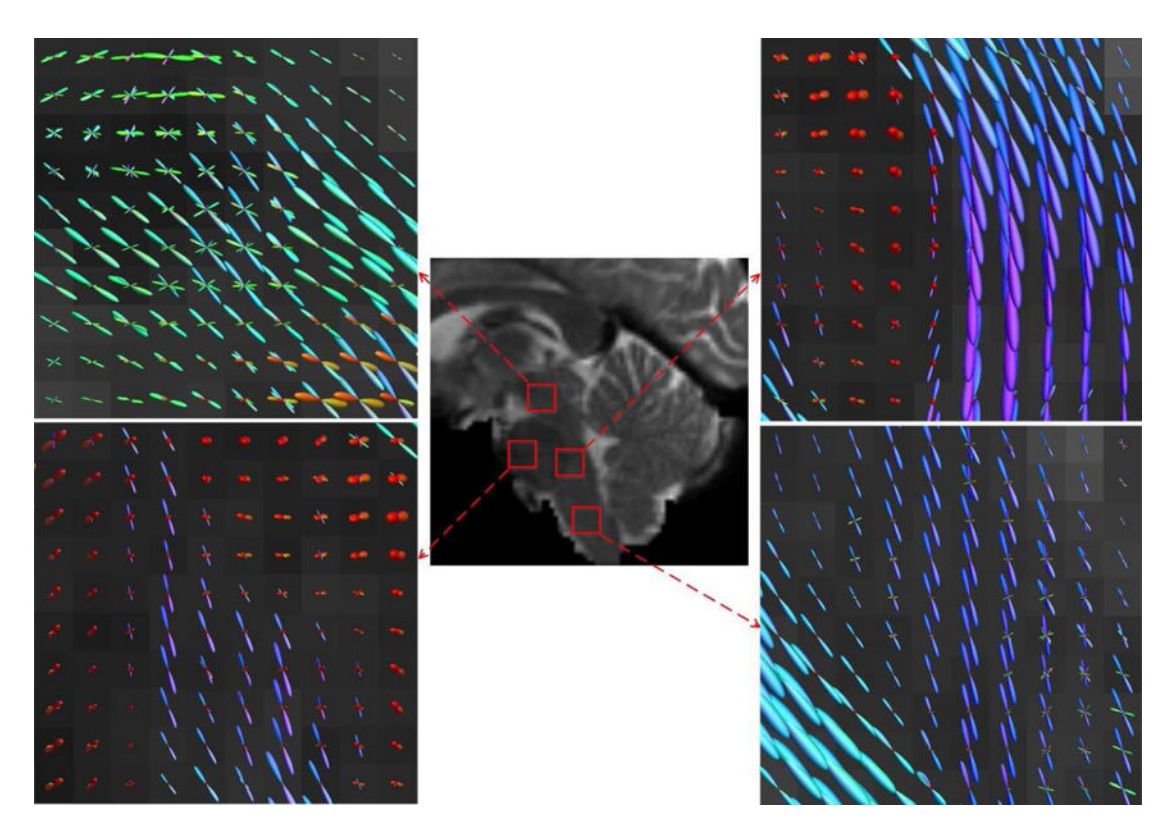


Figure 2.Reconstructed FODs in four brainstem ROIs (red boxes in the middle panel) of an HCP subject with high quality dMRI data. Top left: midbrain; bottom left: ventral pons; top right: dorsal pons; bottom right: medulla oblongata.

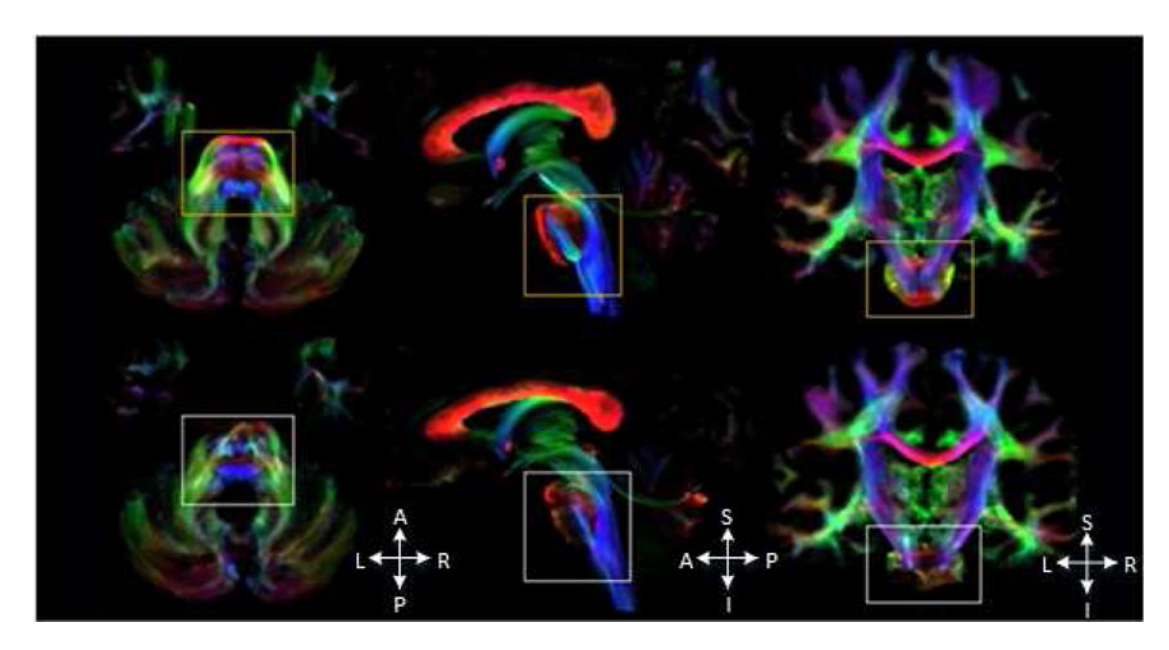


Figure 3.

TDI data from two representative HCP subjects with good (top row) and unsatisfactory distortion correction (bottom row). The brainstem region is viewed in transverse (left), sagittal (middle) and coronal planes (right). Spatial orientations are marked in each column: left (L), right (R), anterior (A), posterior (P), superior (S) and inferior (I).

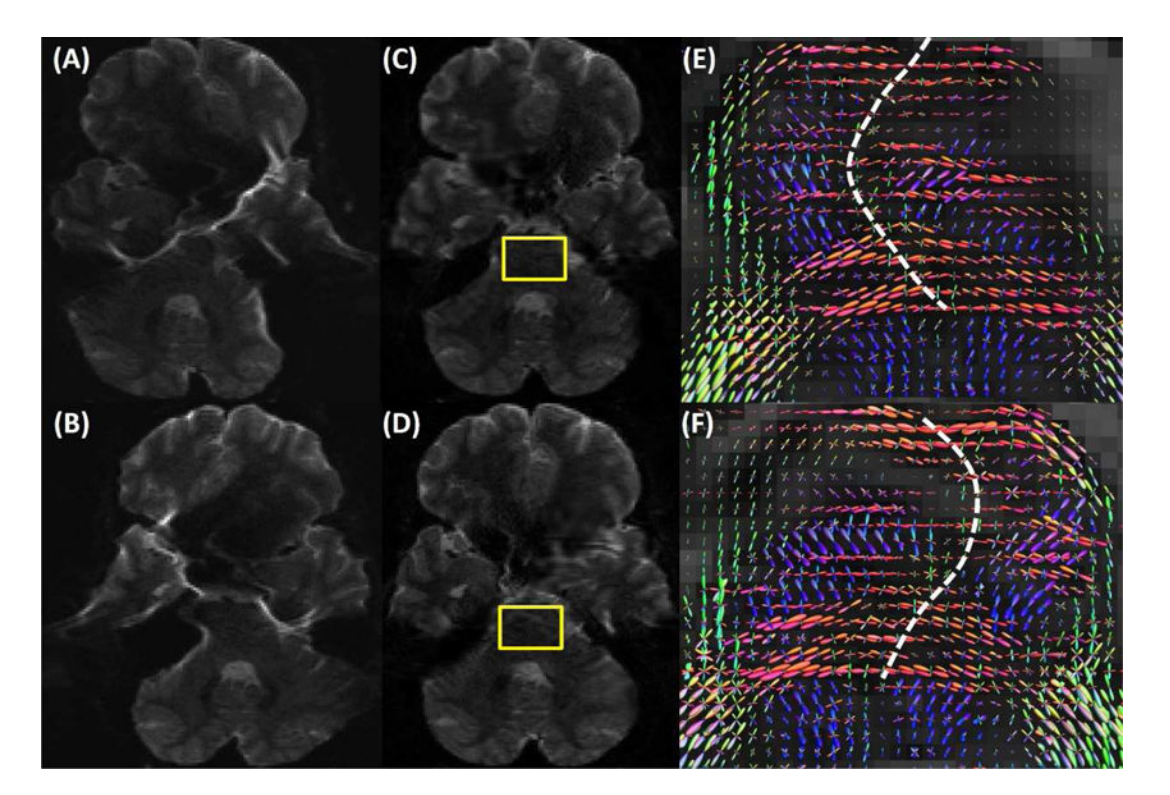


Figure 4. Quality evaluation of the susceptibility distortion correction in preprocessed HCP data. The B0 images collected with the R/L (A) and L/R (B) PE. The corresponding "undistorted" B0 images after the application of distortion correction are shown in (C) and (D). FODs of the highlighted region (yellow box) in (C) and (D) are shown in (E) and (F), respectively. The middle line of the pons is highlighted with the dashed white line for a clear visualization of the residual distortion along the horizontal direction in the preprocessed images.

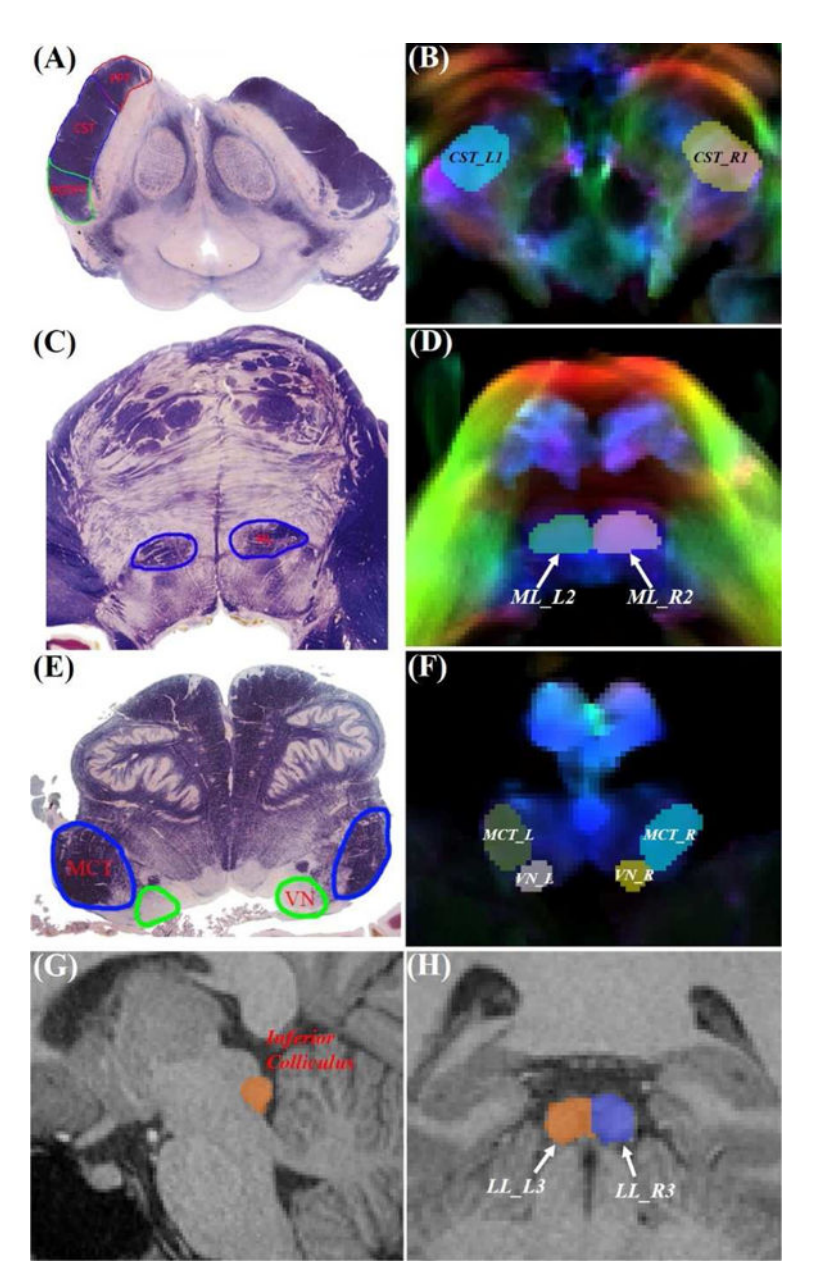


Figure 5.

Examples of manually delineated ROIs of an HCP subject for brainstem bundle reconstruction. Histological sections in (A) (C) (E) are from Nolte's human brain atlas (Nolte, 2013) (reproduced with permission). (A) Boundaries of CST, FPT, and POTPT bundles on a stained histology section in the midbrain. (B) The first ROI of left (CST_L1) and right (CST_R1) CST at a comparable slice of the TDI in the midbrain. (C) Boundaries of the ML on a stained histology section in the pons. (D) The second ROI of ML on the left (ML_L2) and right (ML_R2) hemisphere at a comparable slice of the TDI in the pons. (E) Boundaries of the restiform body (MCT) and vestibular nuclei (VN) on a stained histology section in the medulla oblongata. (F) Manually delineated ROIs of MCT and VN on the left (MCT_L, VN_L) and right (MCT_R, VN_R) hemisphere in the medulla oblongata, respectively. (G) Manually delineated inferior colliculus on a sagittal slice of the T1-

weighted MRI. (H) The third ROI of the LL on the left (**LL_L3**) and right hemisphere (**LL_R3**) on a coronal slice of the T1-weighted MRI.

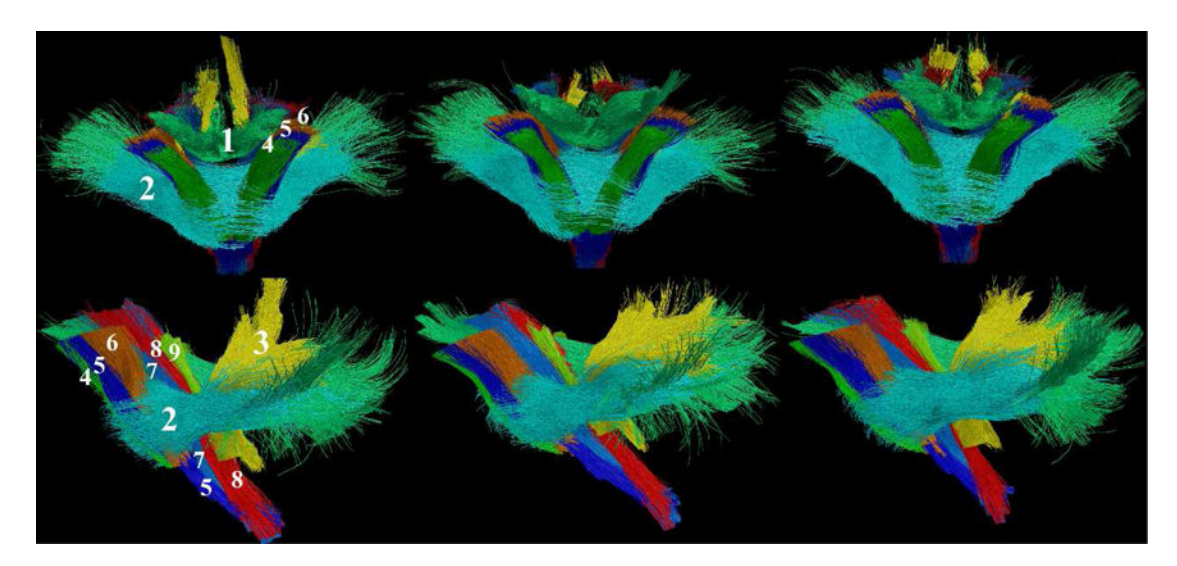


Figure 6. Main brainstem bundles of three HCP subjects are shown from the frontal (top row) and lateral (bottom row) view. The following bundles as annotated on the first subject are visualized. 1. SCP; 2. MCP; 3. ICP; 4. FPT; 5. CST; 6. POTPT; 7. ML; 8. STT; 9. LL. Note that we did not distinguish the left and right hemisphere in our annotation here.

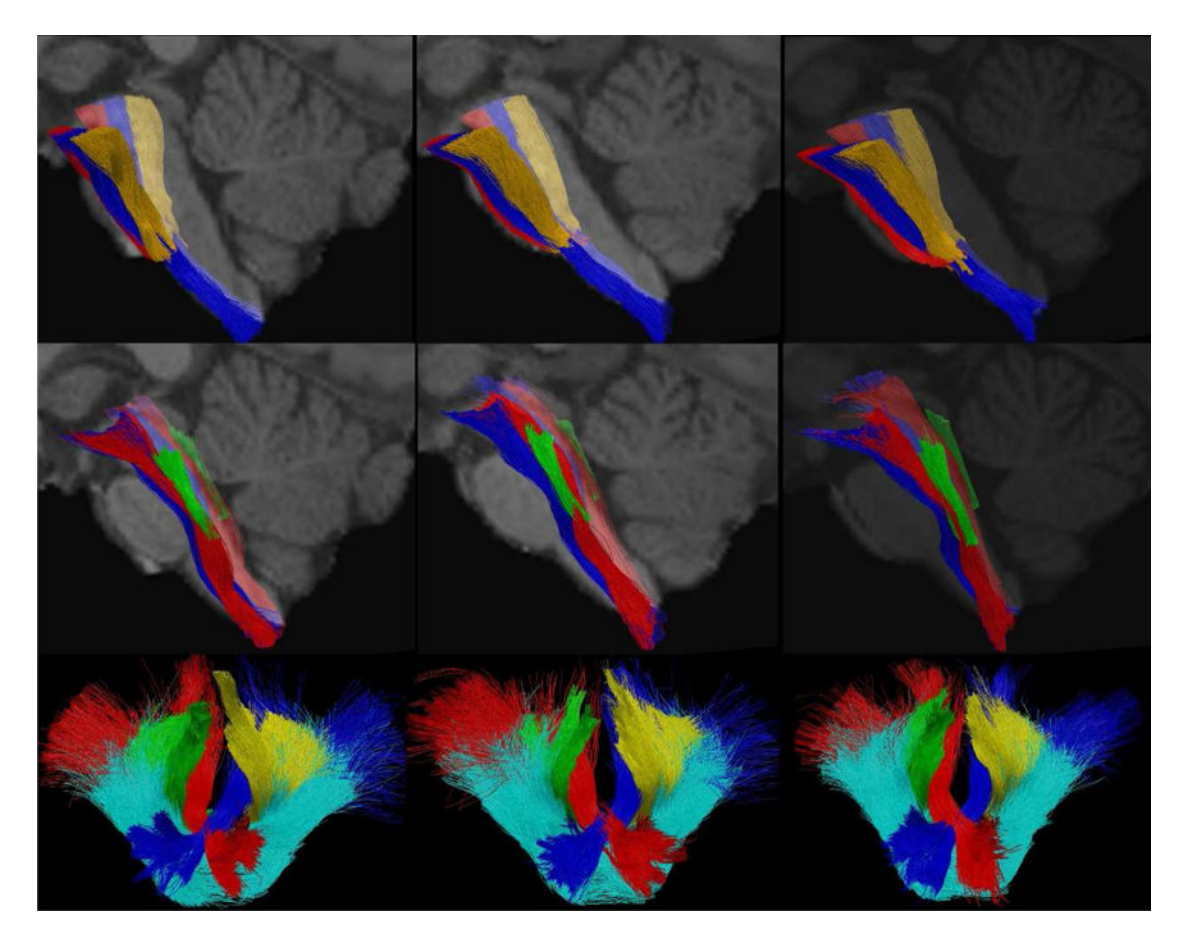


Figure 7.

The brainstem bundles of three HCP subjects are shown in three separate groups. Top row: 6 motor tracts including FPT (red), CST (blue), and POTPT (yellow) on both hemispheres.

Middle row: 6 sensory tracts including ML (blue), STT (red), and LL (green) on both hemispheres. Bottom row: cerebellar peduncles including the left SCP (blue), right SCP (red), MCP (cyan), left ICP (yellow), and right ICP (green).

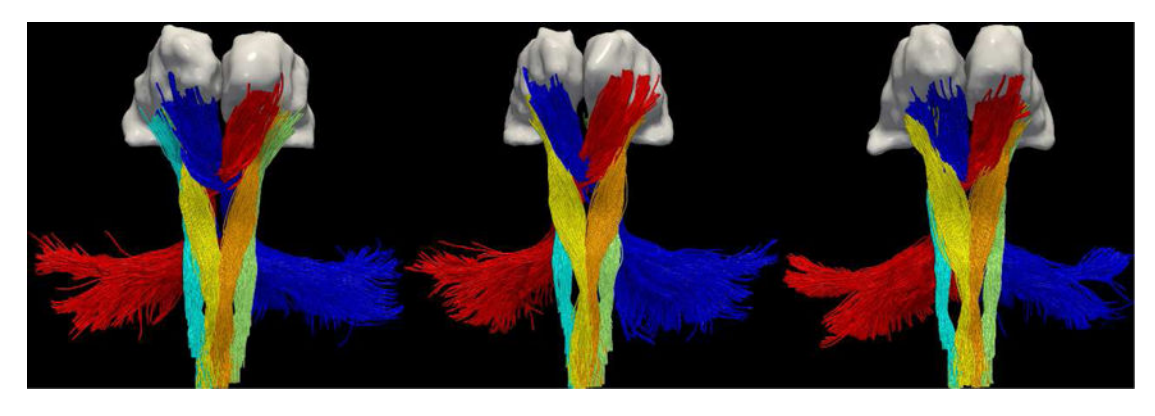


Figure 8.The projection of brainstem bundles onto thalamic surfaces. Results from the same three HCP subjects are shown from the anterior view. Left SCP: blue; right SCP: red; left ML: brown; right ML: yellow; left STT: green; right STT: cyan.

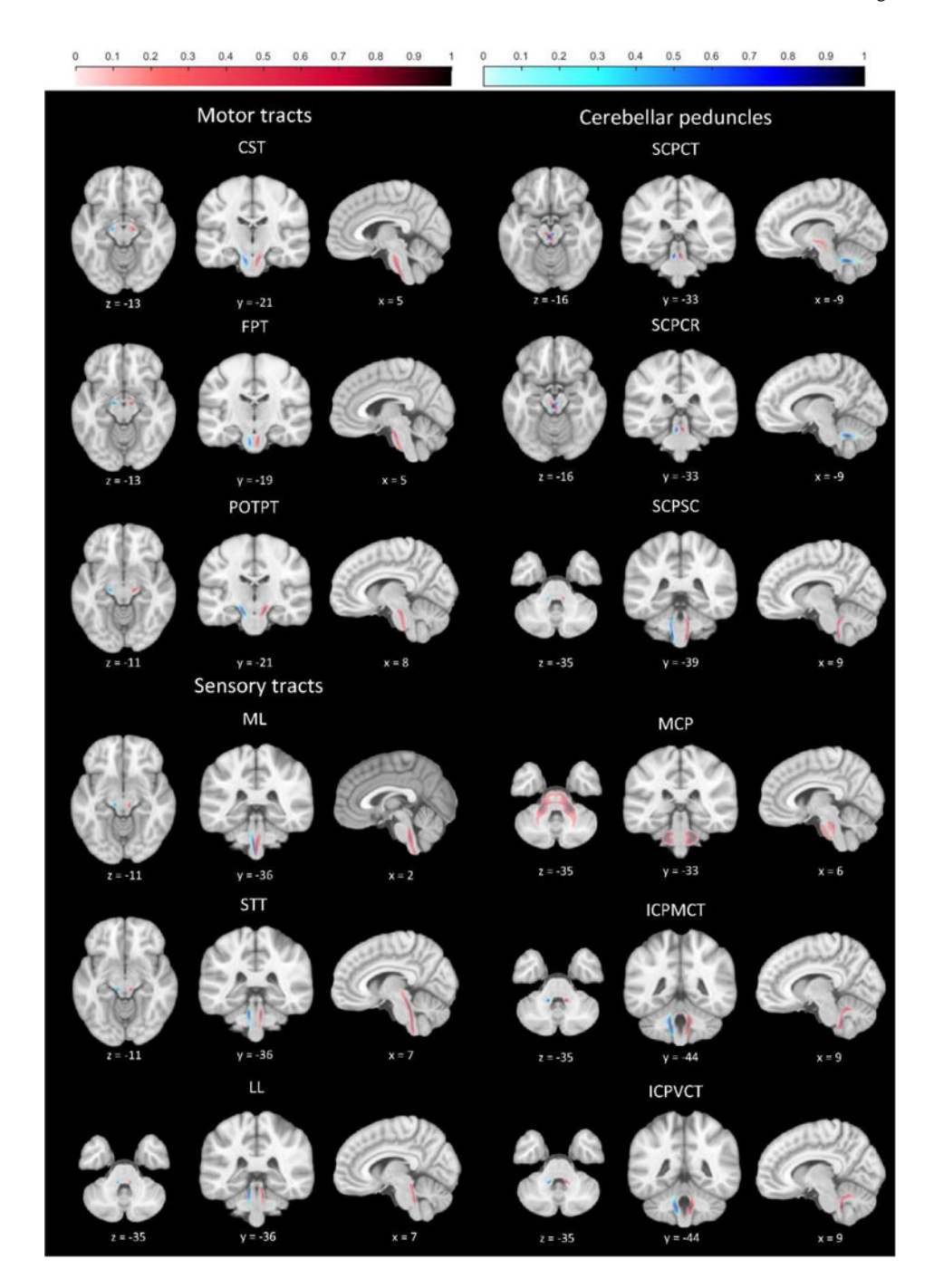


Figure 9. The probabilistic atlases of all 23 brainstem bundles in the standard MNI152 space. Images are displayed in the neurological convention. For all bundles except MCP, right tracts are marked red and left tracts are displayed in blue.

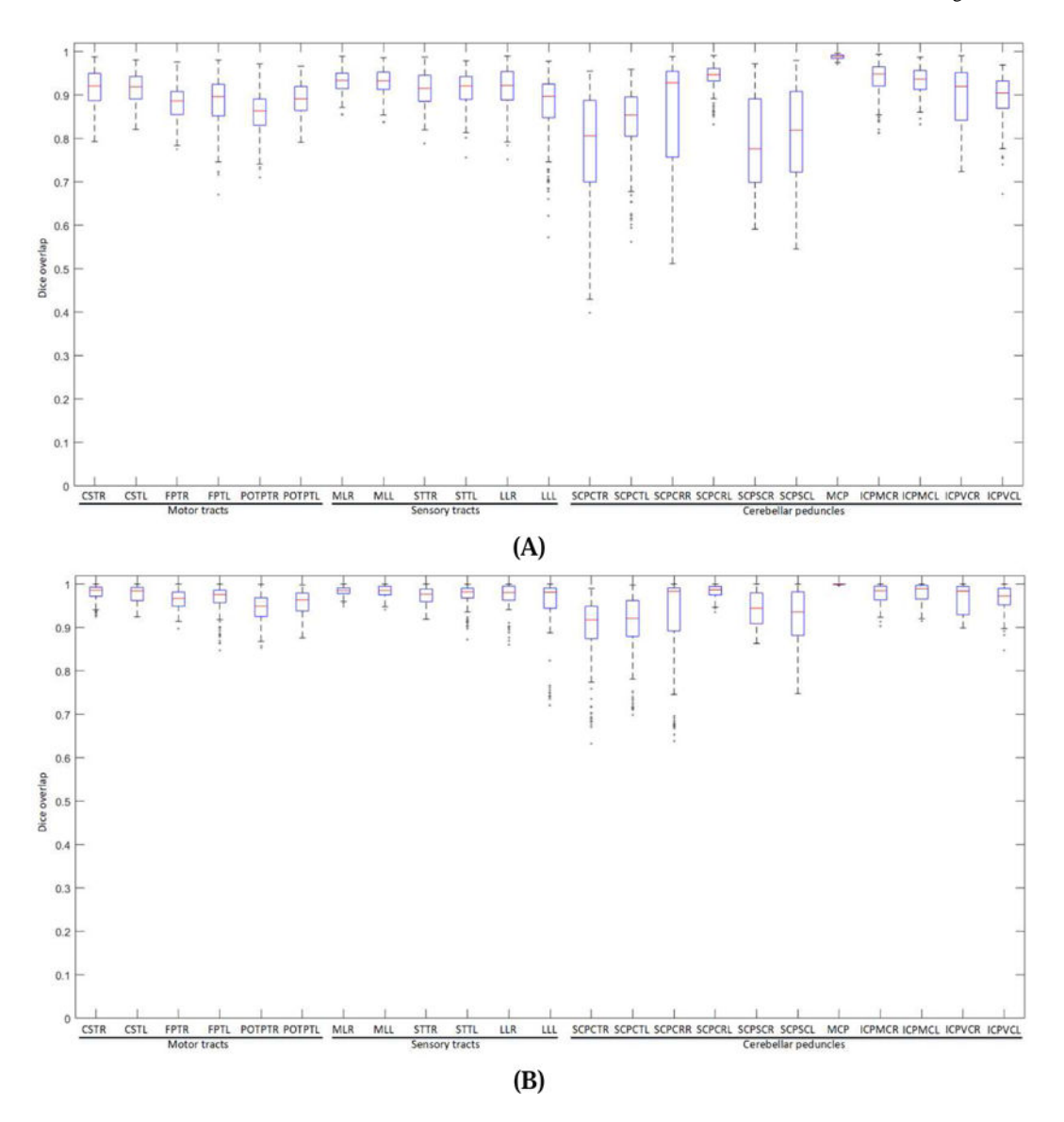


Figure 10.Box plots of pairwise Dice overlap coefficients of the 23 brainstem bundles across 20 HCP subjects in the MNI152 space at the probability level (A) 10% and (B) 30%, respectively. For all bundles except the MCP, the left and right bundles were computed separately.

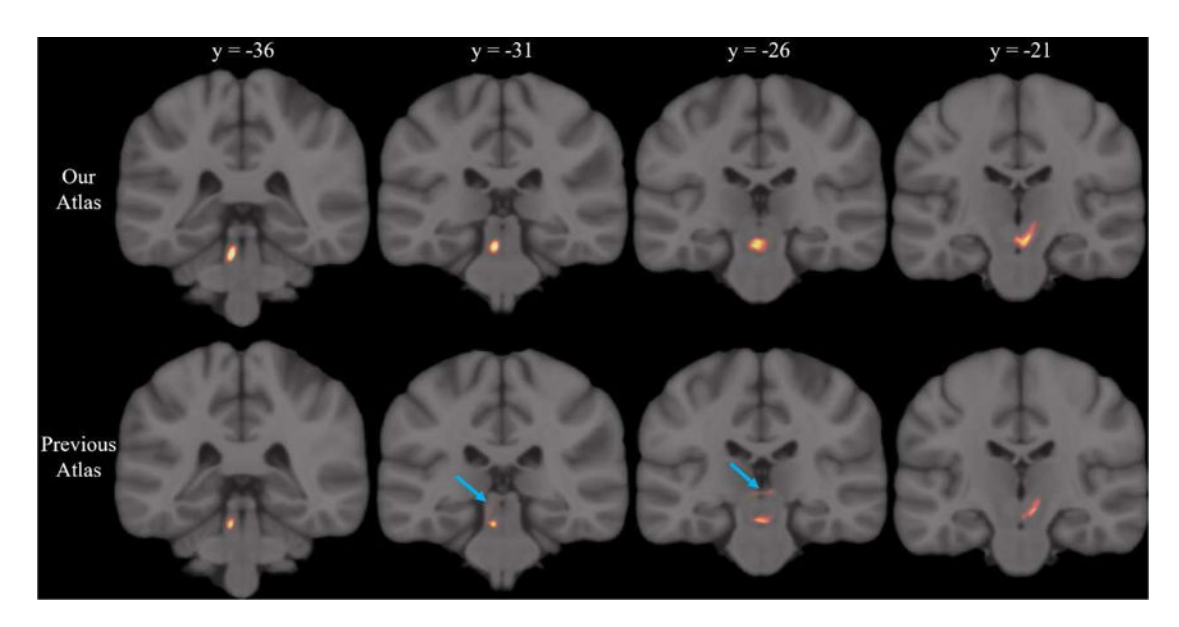


Figure 11. A comparison of the atlas for the left SCP that projects to the right thalamus. Probabilistic distribution of both bundle atlases were overlaid on four coronal slices of the MNI 152 atlas using the same heat map. These four slices cover the SCP from entering the brainstem until reaching the thalamus. The spurious branch of the previous atlas was highlighted with the blue arrow in the 2^{nd} and 3^{rd} column.

Table 1

ROI-based protocols for the reconstruction of 23 brainstem bundles (CST: corticospinal tract; FPT: frontopontine tract; POTPT: parieto-occipito-temporo-pontine tract; ML: medial lemniscus; STT: spinothalamic tract; LL: lateral lemniscus; SCP: superior cerebellar peduncle; SCPCT: cerebellothalamic tract of SCP; SCPCR: cerebellorubral tract of SCP; SCPSC: anterior spino-cerebellar tract of SCP; MCP: middle cerebellar peduncle; ICP: inferior cerebellar peduncle; ICPMCT: ICP tracts from the medulla oblongata to the cerebellum; ICPVCT: vestibulocerebellar tract of ICP). See supplemental material for a detailed description of the ROIs. ROIs in red: tracts stop when they reach this ROI. ROIs in green: tracts start from this ROI.

Fiber bundle	ROI-based tractography protocol
Left CST	$CST_L1 \leftrightarrow CST_L2 \leftrightarrow CST_L3 \leftrightarrow CST_L4 \leftrightarrow CST_L5$
Right CST	$CST_R1 \leftrightarrow \textit{CST_R2} \leftrightarrow \textit{CST_R3} \leftrightarrow \textit{CST_R4} \leftrightarrow \textit{CST_R5}$
Left FPT	$FPT_L1 \leftrightarrow \textit{FPT_L2} \leftrightarrow \textit{FPT_L3} \leftrightarrow \textit{FPT_L4} \leftrightarrow Pons_Medulla~Junction$
Right FPT	$FPT_R1 \leftrightarrow \textit{FPT_R2} \leftrightarrow \textit{FPT_R3} \leftrightarrow \textit{FPT_R4} \leftrightarrow \textit{Pons_Medulla Junction}$
Left POTPT	$POTPT_L1 \leftrightarrow POTPT_L2 \leftrightarrow POTPT_L3 \leftrightarrow POTPT_L4 \leftrightarrow Pons_Medulla Junction$
Right POTPT	$POTPT_R1 \leftrightarrow POTPT_R2 \leftrightarrow POTPT_R3 \leftrightarrow POTPT_R4 \leftrightarrow Pons_Medulla Junction$
Left ML	$ML_LI \leftrightarrow ML_L2 \leftrightarrow ML_L3 \leftrightarrow Left Thalamus$
Right ML	$ML_R1 \leftrightarrow ML_R2 \leftrightarrow ML_R3 \leftrightarrow Right Thalamus$
Left STT	$STT_L1 \leftrightarrow STT_L2 \leftrightarrow STT_L3 \leftrightarrow Left Thalamus$
Right STT	$STT_R1 \leftrightarrow STT_R2 \leftrightarrow STT_R3 \leftrightarrow Right Thalamus$
Left LL	$LL_{-}L1 \leftrightarrow LL_{-}L2 \leftrightarrow LL_{-}L3$
Right LL	$LL_{-}R1 \leftrightarrow LL_{-}R2 \leftrightarrow LL_{-}R3$
Left SCPCT	$SCP_L1 \leftrightarrow (RN_R + SCP_R2) \leftrightarrow RightThalamus$
Right SCPCT	$SCPRI \leftrightarrow (RN_L + SCP_L2) \leftrightarrow Left Thalamus$
Left SCPCR	$SCP_LI \leftrightarrow RN_R$
Right SCPCR	$SCP_RI \leftrightarrow RN_LL$
Left SCPSC	$SCP_L3 \leftrightarrow SCP_L1$
Right SCPSC	$SCP_R3 \leftrightarrow SCP_R1$
МСР	$\begin{array}{c} \textit{1. MCP_1} \leftrightarrow \textit{MCP_L2} \leftrightarrow \textit{MCP_L3} \\ \textit{2. MCP_1} \leftrightarrow \textit{MCP_R2} \leftrightarrow \textit{MCP_R3} \\ \textit{3. MCP_L3} \leftrightarrow \textit{MCP_L2} \leftrightarrow \textit{MCP_1} \leftrightarrow \textit{MCP_R2} \leftrightarrow \textit{MCP_R3} \end{array}$
Left ICPMCT	$MCT_L \leftrightarrow ICP_L1 \leftrightarrow ICP_L2$
Right ICPMCT	$MCT_R \leftrightarrow ICP_R 1 \leftrightarrow ICP_R 2$

Tang et al.

 Fiber bundle
 ROI-based tractography protocol

 Left ICPVCT
 $VN_-L \leftrightarrow ICP_-L1 \leftrightarrow ICP_-L2$

 Right ICPVCT
 $VN_-R \leftrightarrow ICP_-R1 \leftrightarrow ICP_-R2$

Page 29